

1 **Large-Scale Vertical Velocity, Diabatic Heating and Drying**
2 **Profiles Associated with Seasonal and Diurnal Variations of**
3 **Convective Systems Observed in the GoAmazon2014/5**
4 **Experiment**

5 Shuaiqi Tang¹, Shaocheng Xie¹, Yunyan Zhang¹, Minghua Zhang², Courtney Schumacher³,
6 Hannah Upton³, Michael P. Jensen⁴, Karen L. Johnson⁴, Meng Wang⁴, Maike Ahlgrimm⁵, Zhe
7 Feng⁶, Patrick Minnis⁷ and Mandana Thieman⁸

8 ¹Lawrence Livermore National Laboratory, Livermore, CA, 94550, USA

9 ²School of Marine and Atmospheric Sciences, Stony Brook University, Stony Brook, NY, 11794, USA

10 ³Department of Atmospheric Sciences, Texas A&M University, College Station, TX, 77843, USA

11 ⁴Brookhaven National Laboratory, Upton, NY, 11973, USA

12 ⁵European Centre for Medium-Range Weather Forecasts, Shinfield Park, Reading RG2 9AX, United Kingdom

13 ⁶Pacific Northwest National Laboratory, Richland, Washington, 99354, USA

14 ⁷NASA Langley Research Center, Hampton, VA, 23681, USA

15 ⁸Science Systems and Applications, Inc, Hampton, VA 23666, USA

16 *Correspondence to:* Shuaiqi Tang (tang32@llnl.gov)

17 **Abstract.** This study describes the characteristics of large-scale vertical velocity, apparent
18 heating source (Q_1) and apparent moisture sink (Q_2) profiles associated with seasonal and diurnal
19 variations of convective systems observed during the two intensive operational periods (IOPs)
20 that was conducted from 15 February to 26 March 2014 (wet season) and from 1 September to
21 10 October 2014 (dry season) near Manaus, Brazil, during the Green Ocean Amazon
22 (GoAmazon2014/5) experiment. The derived large-scale fields have large diurnal variations
23 according to convective activity in the GoAmazon region and the morning profiles show distinct
24 differences between the dry and wet seasons. In the wet season, propagating convective systems
25 originating far from the GoAmazon region are often seen in the early morning, while in the dry
26 season, they are rarely observed. Afternoon convective systems due to solar heating are
27 frequently seen in both seasons. Accordingly, in the morning, there is strong upward motion and
28 associated heating and drying throughout the entire troposphere in the wet season, which is
29 limited to lower levels in the dry season. In the afternoon, both seasons exhibit weak heating and

30 strong moistening in the boundary layer related to the vertical convergence of eddy fluxes. A set
31 of case studies of three typical types of convective systems occurring in Amazonia - i.e., locally-
32 occurring systems, coastal-occurring systems and basin-occurring systems - is also conducted to
33 investigate the variability of the large-scale environment with different types of convective
34 systems.

35 **1. Introduction**

36 Amazonia is one of the major tropical convective regions in the global climate system. It
37 provides moisture to the global hydrological cycle and energy to drive the global atmospheric
38 circulation. Understanding convective systems over the Amazon region through observations is
39 important for understanding and simulating global circulation and climate. However, most of
40 Amazonia is covered by tropical forest with only a few observational sites. In order to collect
41 the observations needed to improve our understanding of convective systems over Amazonia,
42 several major field campaigns have been conducted in this area such as the Amazon Boundary
43 Layer Experiments (Harriss et al., 1988; Harriss et al., 1990), the Large-Scale Biosphere-
44 Atmosphere Experiment in Amazonia (LBA) (Silva Dias et al., 2002b), and the CHUVA project
45 (Machado et al., 2014).

46 Recently, an internationally collaborative experiment, the Observations and Modeling of
47 the Green Ocean Amazon (GoAmazon2014/5) (Martin et al., 2016), was conducted in the region
48 around Manaus, Brazil from January 2014 to December 2015 with a focus on the aerosol and
49 cloud life cycles and aerosol-cloud-precipitation interactions over tropical rainforests. Two 40-
50 day Intensive Operational Periods (IOPs) were conducted in 2014 to investigate the seasonal
51 variations of clouds and aerosols, as well as their interactions. IOP1 took place from 15
52 February to 26 March 2014 during the wet season, and IOP2 took place from 1 September to 10
53 October 2014 during the dry season. The goal of this study is to document and understand the
54 seasonal variability and diurnal cycle of large-scale vertical velocity, heat and moisture budgets
55 associated with the convective systems observed during the two IOPs in the GoAmazon2014/5
56 experiment.

57 The Amazon region has a significant seasonal variation in precipitation amount. Rainfall
58 is approximately 300 mm per month during the wet season while it is close to 100 mm per month
59 during the dry season (Tanaka et al., 2014). Many studies have examined the seasonal variation
60 of clouds and precipitation in Amazonia (e.g. Harriss et al., 1988; Harriss et al., 1990; Fu et al.,
61 1999; Fu et al., 2001; Schumacher and Houze, 2003; Machado et al., 2004; Li et al., 2006; Nobre
62 et al., 2009; Marengo et al., 2012; Filho et al., 2015). Compared to the large variation in clouds
63 and rainfall, the seasonal variation in CAPE is small (Machado et al., 2004; Martin et al., 2016).
64 Martin et al. (2016) suggests that small perturbations in the large-scale circulation can drive
65 dramatic changes in hydrological fields in this region. Few studies, however, have studied the
66 seasonal variation of the diabatic heating and drying structures associated with the convective
67 systems in the Amazon region.

68 The diurnal cycle of the atmosphere is an important feature that is poorly simulated in
69 climate models. Many efforts have been made to observe and to understand the diurnal cycle
70 over the Amazon basin using surface observations (e.g. Harriss et al., 1990; Cutrim et al., 2000;
71 Machado et al., 2004; Tanaka et al., 2014) or satellite data (e.g. Minnis and Harrison, 1984;
72 Greco et al., 1990; Janowiak et al., 2005; Burleyson et al., 2016). The diurnal cycle over the
73 Amazon basin is complex because it is affected by three types of convective systems: locally-
74 occurring systems (LOS) generated locally in the form of small convective cells (area less than
75 1000 km²) with short life time (on the order of 1 hour), coastal-occurring systems (COS)
76 initialized at the northeast coast of Brazil by the sea-breeze and propagating inland as squall lines,
77 and basin-occurring systems (BOS) initialized in the Amazon basin in the form of mesoscale
78 convective systems (MCS) with areas larger than 1000 km² (Greco et al., 1990). These systems
79 reach Manaus, near the center of the Amazon basin, at different times of the day, causing a broad

80 peak of precipitation from morning to early afternoon (e.g. Machado et al., 2004; Tanaka et al.,
81 2014; Burleyson et al., 2016). Schumacher et al. (2007) examined the diurnal cycle of the large-
82 scale heating budget in the southwest Amazon during LBA, but used only two profiles per day,
83 which do not capture the rapidly changing environment. In addition, the diurnal cycle over the
84 highly deforested southwest Amazon is not necessarily representative of the more pristine central
85 Amazonian rainforest.

86 In this study we use data collected from the comprehensive GoAmazon2014/5 field
87 campaign to examine the seasonal and diurnal variations of the large-scale vertical velocity and
88 heat and moisture budgets associated with the convective systems that occur in central Amazonia.
89 Section 2 provides details of the data and method used to derive the large-scale profiles for the
90 GoAmazon2014/5 experiment. Section 3 describes the synoptic conditions for the two IOPs.
91 Sections 4 and 5 show the seasonal variation and diurnal cycle of the large-scale fields,
92 respectively. Section 6 further investigates three selected cases representing different types of
93 convective systems in the wet season. The summary and discussion are given in Section 7.

94

95 **2. Data and Method**

96 Due to the lack of an appropriate sounding array to capture the divergence and advection
97 fields in the analysis domain, the large-scale vertical velocity and budgets analyzed in this study
98 were derived by using, as a first guess, the European Centre for Medium-Range Weather
99 Forecasts (ECMWF) analysis data that are subsequently constrained with domain averaged
100 surface and top of atmosphere (TOA) observations. The upper-level fields from ECMWF
101 analysis data are adjusted to conserve the vertical integration of mass, moisture and dry static

102 energy through a constrained variational analysis technique described in Zhang and Lin (1997)
103 and Zhang et al. (2001). As indicated in Xie et al. (2004), the use of the surface and TOA
104 observations as constraints improves the quality of the large-scale vertical velocity and budgets
105 in operational analysis data and makes the data suitable for budget analysis and cloud modeling
106 studies. An important by-product of this study is the derived large-scale forcing data (ARM
107 Climate Research Facility, 2001) supporting modeling studies, which are available to the
108 community at the Atmospheric Radiation Measurement (ARM) program Archive
109 (http://iop.archive.arm.gov/arm-iop/0eval-data/xie/scm-forcing/iop_at_mao/).

110 Figure 1 shows the location of the GoAmazon2014/5 experiment and the analysis domain
111 (the red octagon, referred to as the GoAmazon domain) used in this study, which is about 110
112 km in radius. The observational research sites and major cities near the region are also shown on
113 the map. The required surface and TOA fluxes as the constraints for the variational analysis are
114 constructed as follows. The precipitation used in this study is derived from the System for the
115 Protection of Amazonia (SIPAM) S-band (10 cm wavelength) radar operated at Ponta Pelada
116 airport, the center of the GoAmazon domain. The SIPAM radar reflectivity constant altitude
117 plan position indicator (CAPPI) at 2.5 km above ground was used to generate the rain rate
118 products using a single Z-R relation of $Z = 174.8R^{1.56}$ derived from Joss-Waldvogel disdrometer
119 data obtained by the CHUVA campaign near Manacapuru during the wet season of early 2014.
120 Other surface constraint variables, such as surface radiative fluxes and latent and sensible heat
121 fluxes, are obtained from the broadband radiometer (ARM Climate Research Facility, 1994) and
122 eddy correlation flux measurement system (ARM Climate Research Facility, 2003) at the ARM
123 Mobile Facility site near Manacapuru (3.213°S, 60.598°W; “ARM site” in Figure 1).
124 Observations of latent and sensible heat fluxes at two other Brazilian research sites - K34 (“ZF2”

125 in Figure 1) and the Amazon Tall Tower Observatory (“ATTO” in Figure 1) - are also used. The
126 TOA measurements of broadband radiative fluxes are estimated from the Thirteenth
127 Geostationary Operational Environmental Satellite (GOES-13) 4-km visible (0.65 μm) and
128 infrared window (10.8 μm) radiances using the narrowband-to-broadband (NB-BB) conversion
129 method of Minnis and Smith (1998) that was updated similar to Khaiyer et al. (2010), with some
130 modifications to more closely match those measured by the Clouds and Earth’s Radiant Energy
131 System (CERES) on the Aqua and Terra satellite. The radar precipitation and satellite data are
132 3-hourly average over the analysis domain. The surface radiative fluxes and latent and sensible
133 heat fluxes are first averaged into 3-hour resolution. Then we use the Cressman’s objective
134 analysis method (Cressman, 1959) to incorporate these limited number of observations with the
135 ECMWF gridded analysis and calculate the domain mean, so that the domain-mean surface
136 fluxes can better represent the entire domain. The derived large-scale vertical velocity and
137 budgets are thus representing a 3-hour average over analysis domain. The vertical resolution is
138 25 hPa.

139

140 **3. Background of Synoptic Conditions**

141 The IOP-averaged sea-level pressure and 10-meter horizontal winds from ERA-Interim
142 reanalysis (Dee et al., 2011) are plotted in Figure 2. During IOP1, the Atlantic Intertropical
143 Convergence Zone (ITCZ) was located near the Equator; while during IOP2, it was located near
144 10°N. A fourteen-day trajectory study shows that the air masses over Manaus typically come
145 from the Northern Hemisphere during IOP1 and from the Southern Hemisphere during IOP2
146 (Martin et al., 2016). The top three rows of Figure 3 show the domain-averaged zonal (u) wind,

147 meridional (v) wind, and relative humidity relative to liquid water, from the adjusted ECMWF
148 analysis. Consistent with those derived from radiosonde data in Martin et al. (2016), IOP1 was
149 dominated by northeasterly winds in the lower troposphere, with moist air throughout the
150 troposphere; IOP2 was dominated by easterly winds in the lower troposphere, with a dry free
151 troposphere.

152 The cloud frequency and domain-mean precipitation observed during IOP1 and IOP2 are
153 shown in the remaining two rows of Figure 3. The cloud frequency was derived from the Active
154 Remote Sensing of Clouds (ARSCL) (Kollias et al., 2007) product, which uses a combination of
155 the 95GHz W-band ARM cloud radar (WACR), micropulse lidar (MPL), and ceilometer located
156 at the ARM site pointing upward to determine a best-estimate cloud mask above the ARM site
157 with 5-second temporal and 30-meter vertical resolution. The ARSCL product leverages each
158 instrument's strengths: the WACR penetrates non-precipitating and weakly precipitating thick
159 clouds, the MPL is sensitive to thin clouds, and the ceilometer reliably detects cloud base. The
160 ARSCL-derived cloud mask data were then used to produce 3-hourly cloud frequencies
161 following the method described in Xie et al. (2010b). The wet season has more cloud and
162 precipitation events than the dry season. However, the convective systems in the dry season are
163 typically more intense than those occurring in the wet season (Giangrande et al., 2016).
164 Compared to 15-year climatology, the precipitation around Manaus during 2014 has a positive
165 anomaly in IOP1 and negative anomaly in IOP2 (Burleyson et al., 2016; Martin et al., 2016).
166 Nevertheless, the annual cycle in 2014 is still broadly representative of the climatology
167 (Burleyson et al., 2016).

168

169 **4. Seasonal Variation**

170 In this section, we focus on the contrast between the dry and wet season large-scale
171 vertical velocity and energy and moisture budgets. The upper row of Figure 4 shows the
172 temporal evolution of large-scale vertical velocity in IOP1 (wet season, left) and IOP2 (dry
173 season, right), and the IOP-mean profiles are shown as the black solid lines in the bottom row.
174 We also define rainy (black dotted lines) and non-rain periods (gray lines) using a threshold of
175 0.2 mm hr^{-1} . A value of 0.2 mm hr^{-1} rather than 0 mm hr^{-1} is used because in some cases ground
176 clutter in the SIPAM radar data may be misinterpreted as light precipitation. Changing the
177 threshold affects the magnitude of the vertical profiles but does not change the seasonal contrast
178 and the results of this study. Using this threshold, the percentage of the rainy period to the entire
179 IOP is 36.9% for IOP1, but is 17.8% for IOP2, indicating that the rain frequency is an important
180 factor impacting the seasonal mean contrast. The red and blue lines represent the mean profiles
181 of morning (at 5 local time (LT)) precipitation systems and afternoon (at 14 LT) precipitation
182 systems, respectively, which will be discussed in Section 5.

183 The non-rain vertical velocity profiles are relatively weak, with downward motion
184 dominating in the upper troposphere during both dry and wet seasons. The rainy vertical
185 velocity profiles show strong upward motion throughout the troposphere during both IOPs, but
186 the level of maximum upward motion is different. The upward motion during the rainy period of
187 IOP1 has a broad peak structure from ~ 700 to 300 hPa with the maximum at $\sim 350 \text{ hPa}$. The
188 350-hPa upward motion peak is consistent with that shown in the Tropical Ocean and Global
189 Atmosphere Coupled Ocean-Atmosphere Response Experiment (TOGA COARE) (Lin and
190 Johnson, 1996), but lower than the peak of $\sim 265 \text{ hPa}$ observed in the Tropical Warm Pool-
191 International Cloud Experiment (TWP-ICE) (Xie et al., 2010a). The upward motion during the

192 IOP2 rainy period also has a broad peak but the maximum is at a much lower level (~550 hPa)
 193 than in IOP1. Because the frequency of the rainy period is higher in IOP1 than in IOP2, the IOP-
 194 mean upward motion is stronger during IOP1 but weaker and limited to the lower troposphere
 195 during IOP2. As discussed in the next section, the difference in morning precipitation systems
 196 largely contributes to the seasonal contrast in the vertical velocity profiles between the wet and
 197 dry seasons.

198 Figures 5 and 6 show the temporal evolution and IOP-mean of apparent heating Q_1 and
 199 apparent drying Q_2 profiles, respectively. Q_1 and Q_2 were first introduced by Yanai et al. (1973)
 200 to estimate the diabatic processes:

$$\begin{aligned}
 Q_1 &= \frac{1}{C_p} \left(\frac{\partial \bar{s}}{\partial t} + \bar{\mathbf{V}} \cdot \nabla \bar{s} + \bar{\omega} \frac{\partial \bar{s}}{\partial p} \right) \\
 &= \frac{1}{C_p} \left(Q_{rad} + L_v (c - e) - \frac{\partial \overline{\omega' s'}}{\partial p} \right) ,
 \end{aligned}$$

201

202 (1)

$$\begin{aligned}
 Q_2 &= -\frac{L_v}{C_p} \left(\frac{\partial \bar{q}}{\partial t} + \bar{\mathbf{V}} \cdot \nabla \bar{q} + \bar{\omega} \frac{\partial \bar{q}}{\partial p} \right) \\
 &= \frac{L_v}{C_p} \left(c - e + \frac{\partial \overline{\omega' q'}}{\partial p} \right) ,
 \end{aligned}$$

203

204 (2)

205 where $s = C_p T + gz$ is the dry static energy and C_p is the specific heat for dry air in constant
 206 pressure; q is water vapor mixing ratio; $\bar{\mathbf{V}}$ is horizontal wind vector; $\bar{\omega}$ is vertical velocity in
 207 pressure coordinate; Q_{rad} is radiative heating; $L_v (c - e)$ is the latent heat from water
 208 condensation and evaporation (in general it also includes the latent heat and water vapor change

209 from ice phase change); the overbar refers to a horizontal average and the prime refers to a
210 deviation from the average. Q_1 and Q_2 are calculated from the large-scale dynamics (the first
211 lines of the equations) and represent the unresolved physical heat sources and moisture sinks (the
212 second lines). Because the thermodynamic equation and water vapor conservation equation are
213 explicitly satisfied in the variational analysis and the observed precipitation is used as the constraint, the
214 vertical integral of $Q_1 - Q_{rad}$ and vertical integral of Q_2 are consistent with the observed precipitation rate
215 implicitly. The vertical distributions of heating and drying profiles are important to the large-
216 scale circulation as discussed in many other studies (e.g. Hartmann et al., 1984; Lau and Peng,
217 1987; Puri, 1987; Hack and Schubert, 1990).

218 Overall, the magnitude of Q_1 and Q_2 are consistent with Schumacher et al. (2007) for
219 LBA at southwestern Brazilian Amazon but much smaller than Greco et al. (1994) at Manaus
220 region. The much larger magnitude in Greco et al. (1994) is likely because it is a case study of
221 one day. The peak height in this study is also lower than the other two studies, indicating that
222 our cases contain more shallow cumulus and convections with low-level heating and drying.

223 Similar to the profiles of vertical velocity, non-rain Q_1 and Q_2 profile magnitudes in both
224 IOPs are weak with small amounts of heating and moistening below 600 hPa indicative of non-
225 precipitating or very weakly precipitating shallow cumulus and congestus clouds (Schumacher et
226 al., 2008). Rainy period Q_1 and Q_2 profiles show strong heating and drying throughout the
227 troposphere during both IOPs associated with deep convection, and both of them have double
228 peak structures that vary between dry and wet seasons. Q_1 during IOP1 has a broad primary
229 peak between 600 and 400 hPa, while the primary Q_1 peak during IOP2 maximizes more sharply
230 at 550 hPa. The secondary peaks of Q_1 are at ~ 750 hPa in both IOPs. The peaks of Q_2 in IOP1
231 (at 500 and 750 hPa) are higher than those in IOP2 (at 650 and 800 hPa). The double peak

232 features of Q_1 and Q_2 are likely due to different physical processes. For Q_1 , previous studies
233 (Johnson, 1984; Schumacher et al., 2007) interpreted the double peaks as a result from shallow
234 cumulus in lower level and deep convection or MCS in middle to upper level, although
235 sometimes they superposed as one peak (Johnson, 1984). Moreover, latent cooling due to ice
236 melting in the stratiform region may also contribute to the local minimum of Q_1 which, in some
237 field campaigns, is only shown as an inflection (Johnson et al., 2016). Nevertheless, the local
238 minimum or the inflection usually occurs near the melting level (~ 600 hPa) in many other
239 tropical field campaigns (e.g. Schumacher et al., 2008; Xie et al., 2010a; Ahmed et al., 2016),
240 indicating that the melting level is nearly constant in the tropics. For Q_2 , the double-peak
241 structure is the combined effect of convective (lower peak) and stratiform (higher peak) rain
242 production (Lin and Johnson, 1996). The peak levels for stratiform and convective clouds may
243 vary in different locations and times such as in the two IOPs in this study.

244

245 **5. Diurnal Cycle**

246 The diurnal cycles of domain mean radar-derived precipitation and surface CAPE and
247 convective inhibition (CIN) for both IOPs are plotted in Figure 7. Precipitation in IOP1 extends
248 from early morning to afternoon, consistent with Tanaka et al. (2014). In IOP2, most of the
249 precipitation occurs in the afternoon. The magnitude of afternoon precipitation in IOP2 is just
250 slightly smaller than that in IOP1, but the magnitude of morning precipitation in IOP2 is
251 significantly lower than that in IOP1, indicating that the differences between dry and wet seasons
252 are mainly due to the morning precipitation events. The surface CAPE has similar magnitudes in
253 the daytime during IOP1 and IOP2, but in the early morning it rises later and slower during IOP1

254 than during IOP2, probably because early morning precipitation during IOP1 has released
 255 atmospheric instability. The surface CIN is typically small, especially during IOP1, which is due
 256 to the high surface relative humidity over the Amazon rainforest.

257 The diurnal cycles of cloud frequency, large-scale vertical velocity, Q_1 , Q_2 and
 258 $Q_1 - Q_2 - Q_{rad}$ for IOP1 (left) and IOP2 (right) are shown in Figure 8. Derived from Eq. (1) and
 259 (2),

$$260 \quad Q_1 - Q_2 - Q_{rad} = -\frac{1}{C_p} \frac{\partial \overline{\omega' h'}}{\partial p} \quad (3)$$

261 where $h = s + L_v q$ is the moist static energy, and Q_{rad} is estimated from using the radiative
 262 transfer model in the single-column model of CAM5 (Neale et al., 2012) driven by the large-
 263 scale forcing data derived from this study since it cannot be directly measured and retrievals for
 264 Q_{rad} using observed vertical cloud profiles (Feng et al., 2014) have not been available yet. .
 265 With the freezing and melting processes ignored, $Q_1 - Q_2 - Q_{rad}$ represents the vertical
 266 convergence of h by sub-grid turbulence and cumulus.

267 Consistent with the diurnal cycles of precipitation, the observed clouds and large-scale
 268 vertical velocity differ primarily in the morning between IOP1 and IOP2. In IOP1, the early
 269 morning upward motion peaks at 700 hPa and extends to the upper troposphere around 200 hPa.
 270 The early afternoon upward motion peaks at the upper troposphere and extends above 100 hPa.
 271 Accordingly, clouds are mainly seen between 800 and 500 hPa in the early morning but
 272 throughout the entire troposphere in the afternoon. In IOP2, morning convective systems are
 273 generally limited to the lower levels, as shown by weak upward motion below 600 hPa and
 274 downward motion above. Thus, few clouds are observed in the lower and middle troposphere

275 while some high clouds remain from the previous day's convective activities. The afternoon
276 convective systems are strong and deep in both IOPs, with upward motion in the upper
277 troposphere associated with convective cloud growth and downward motion in the lower
278 troposphere associated with convective downdrafts.

279 Consistent with the clouds and vertical velocity, Figure 8 also shows significant seasonal
280 differences of Q_1 and Q_2 profiles in the morning, with heating and drying extending to the upper
281 troposphere in IOP1 but cooling and moistening above 600-650 hPa in IOP2. In the afternoon,
282 both IOPs show strong heating and drying in the middle and upper troposphere with weak
283 heating and strong moistening occurring below 700 hPa. The low-level heating and moistening
284 feature has been observed in trade wind regimes during westerly wind bursts and monsoon break
285 periods (Nitta and Esbensen, 1974; Lin and Johnson, 1996; Johnson and Lin, 1997; Xie et al.,
286 2010a), in which the vertical convergence of eddy fluxes and detrainment of shallow cumulus
287 were considered as the causes. In this study it is also seen in the afternoon precipitating periods
288 (red lines in Figure 5 and 6). To further investigate this feature, $Q_1 - Q_2 - Q_{rad}$ is shown in the
289 last row of Figure 8. Two positive $Q_1 - Q_2 - Q_{rad}$ centers are seen during daytime at ~750 to 950
290 hPa and ~250 to 550 hPa, respectively. It is likely that the positive $Q_1 - Q_2 - Q_{rad}$ in the lower
291 level (below 600 hPa) is mainly due to the vertical convergence of h by boundary layer
292 turbulence and shallow cumulus. The positive $Q_1 - Q_2 - Q_{rad}$ in the upper troposphere (above
293 600 hPa) may be due to the vertical convergence of h by deep convective process. Note that
294 $Q_1 - Q_2 - Q_{rad}$ also includes latent heat from ice freezing and melting, which may contribute to
295 the local minimum around 600 hPa.

296

297 **6. Case Studies**

298 A set of case studies is conducted to further understand the large-scale vertical velocity
299 and heat and moisture budgets for the three typical types of convective systems (Greco et al.,
300 1990) that often occur in the wet season in Amazonia: locally-occurring systems (LOS), coastal-
301 occurring systems (COS), and basin-occurring systems (BOS). Previous studies have found that
302 LOS often occur in the afternoon characterized as scattered convections generated through solar
303 heating at the surface, while most COS and BOS are propagating systems associated with mid-
304 level easterlies and westerlies, respectively (e.g. Cifelli et al., 2002; Silva Dias et al., 2002a;
305 Williams et al., 2002), and affect Manaus in the early morning. COS occurring in easterlies are
306 often westward propagating squall-lines with intense leading lines that are more vertically
307 developed. BOS generated in the westerlies are generally less vertically developed MCSs with a
308 broad horizontal area and relatively homogeneous precipitation extending over a long time
309 (Cifelli et al., 2002). Table 1 gives the number of each type of precipitation system observed
310 during the two IOPs, identified from the radar loop (available at
311 https://www.youtube.com/playlist?list=PLVqbwaasmlvtcu2kl_U5RaaNF0kYqW6ua) and the
312 satellite infrared images (available at <http://www-pm.larc.nasa.gov/>). There are some cases in
313 the easterlies identified as BOS because they initiated in the Amazon basin but their structures
314 are more like COS as squall lines. More COS and BOS are seen in IOP1 than in IOP2, but the
315 number of afternoon LOS in IOP1 is just slightly higher than that in IOP2. This again indicates
316 that the frequency of morning propagating convective systems contributes to the variation of the
317 diurnal cycle between the wet and dry seasons.

318 The three selected cases are a LOS starting from 11 LT, 13 March 2014, a COS starting
319 from 23 LT, 20 February 2014 and a BOS starting from 17 LT, 1 March 2014. The times of

320 these events are marked by the black lines in Figure 3. Mid-level wind was dominated by
321 westerlies on 1 March (day 60) and easterlies on 20 February (day 51). Figure 9 shows
322 representative scans of the radar reflectivity at elevation angle of 0.9° for these three cases, as
323 well as the time series of the domain mean precipitation. The LOS case has many small-scale
324 scattered convective cells that last for very short times (typically a couple of hours). Because of
325 the small horizontal coverage of the convective cells, the domain mean precipitation is less than
326 that in the other two cases. The COS case has a clear bow-shape echo indicating a squall line
327 front which moves quickly westward. The BOS case has a larger horizontal area of moderate
328 precipitation with some embedded convective cells. It moves southeastward and lasts more than
329 10 hours over the GoAmazon domain.

330 The point-observed cloud frequency and domain-averaged relative humidity, surface
331 CAPE and CIN, u- and v-winds, large-scale vertical velocity, Q_1 , Q_2 and $Q_1 - Q_2 - Q_{rad}$ for the
332 three cases are shown in Figures 10-12, respectively. For the LOS case, the cloud frequency is
333 much smaller than in the other two cases, since the convective cells have small horizontal extent
334 and only occupy a small portion of the region. A shallow-to-deep transition of convective clouds
335 can be seen. The surface CAPE is large, with weak mid-level winds and moist air at the surface
336 before the convection occurred. Upward motion corresponds to the deep convection, and the
337 magnitude is smaller than in the other two cases, consistent with weaker precipitation. Starting
338 around 9 LT, Q_1 shows diabatic heating throughout the troposphere during the deep convection,
339 while Q_2 shows strong moistening between 750 and 950 hPa and weak drying above that layer.
340 The daytime positive $Q_1 - Q_2 - Q_{rad}$ between 750 and 950 hPa is mainly contributed by negative
341 Q_2 representing vertical convergence of moisture by sub-grid eddies. It can also be seen on
342 many other days during the two IOPs and are similar to the daytime profiles discussed in the

343 diurnal cycle (Section 5). Note that there is a time lag between observed cloud frequency and the
344 domain-averaged large-scale fields, which might be partially due to the fact that the cloud
345 frequency observations were taken from vertically pointing instruments at the ARM site 67.8 km
346 downwind of the center of the GoAmazon domain.

347 The COS (Figure 11) and BOS (Figure 12) cases both show a shallow-to-deep convective
348 cloud transition from the previous evening to late afternoon, with a moist lower-level atmosphere.
349 Both cases have smaller surface CAPE than the LOS case, possibly because the convective
350 systems have released the atmospheric instability in the morning. The COS case passed through
351 the GoAmazon domain around 6 LT in strong mid-level easterlies, with deep clouds and strong
352 upward motion associated with the squall line. Stratiform clouds, associated with weak upward
353 motion, remained in the upper levels until ~18 LT. Condensation from the deep convection
354 contributes to strong diabatic heating and drying throughout the troposphere, while after the
355 passage of the squall line (12-18 LT), there are some stratiform clouds remaining indicated by
356 upper-level heating/drying and lower-level cooling/moistening. The BOS case entered the
357 GoAmazon domain earlier than the COS case. In weak mid-level westerlies and descending
358 mid-to-low-level northerlies, the system moved slowly southeastward and remained in the
359 domain for a longer time. Strong upward motion related to the MCS is seen from 18 to 6 LT.
360 Large diabatic heating and drying related to the strong condensation is also seen. The remnant
361 high clouds were maintained until ~18 LT with precipitation weakening over time. The upper-
362 level heating and drying, lower-level cooling and moistening indicate that there are precipitating
363 stratiform clouds in the upper level and evaporation of precipitation underneath. The negative
364 $Q_1 - Q_2 - Q_{rad}$ in the lower level and the positive $Q_1 - Q_2 - Q_{rad}$ in the upper level are seen in both
365 the COS and BOS case, which indicates lower-level divergence of h and upper-level

366 convergence of h due to moist convective processes, consistent with Tang and Zhang (2015).
367 The lower-level positive $Q_1 - Q_2 - Q_{rad}$ in the afternoon is mainly contributed by the vertical
368 convergence of moisture by sub-grid eddies, similar to that in the LOS case.

369

370 **7. Summary and Discussion**

371 This study presented the characteristics of the seasonal variation and diurnal cycle of the
372 large-scale vertical velocity and diabatic heating (Q_1) and drying (Q_2) profiles for the two IOPs
373 conducted during the GoAmazon2014/5 experiment. A constrained variational analysis method
374 was used to derive the large-scale vertical velocity and Q_1 and Q_2 profiles based on surface and
375 TOA observations and ECMWF analysis. The derived profiles correspond well with observed
376 clouds and precipitation describing convective systems over Amazonia.

377 The large-scale environment over the region near Manaus has distinct seasonal variations
378 and diurnal cycles. The wet season (IOP1) has more frequent precipitation events than the dry
379 season (IOP2), especially in the morning. The large-scale upward motions during rainy periods
380 have similar strength in both IOPs, however, the peak level in IOP1 is much higher than that
381 exhibited in IOP2 (350 hPa vs. 550 hPa). Q_1 and Q_2 both have a double-peak feature during
382 rainy period, but the physical mechanism may be different: the double peak of Q_1 may be due to
383 the combination of shallow and deep convections and latent cooling near the melting level, while
384 the double peak of Q_2 may be due to the different height of convective and stratiform systems.
385 The seasonal contrast is mainly due to the higher occurrence of morning mesoscale convective
386 systems observed during IOP1. In the morning, upward motion peaks at ~ 700 hPa and extends
387 to the upper troposphere during IOP1, while it is limited to the lower levels with downward

388 motion at the upper levels during IOP2. Afternoon convective systems have a higher vertical
389 motion peak than their morning counterparts, and both IOPs show similar vertical structures for
390 the afternoon systems. The large-scale vertical velocity shows upward motion above 700 hPa and
391 downward motion below. Accordingly, Q_1 and Q_2 also exhibit middle and upper level heating
392 and drying related to the deep convection. Below 750 hPa, the profiles show relatively weak
393 heating and strong moistening. This heating and moistening feature is due to the vertical
394 convergence of heat and moisture by sub-grid eddies in the boundary layer.

395 Three cases from IOP1 representing different types of convective systems that often
396 occur in the region were chosen and analyzed in this study: locally-occurring systems (LOS),
397 coastal-occurring systems (COS) and basin-occurring systems (BOS). The LOS case was
398 characterized by many scattered and short-lived convective cells. It had relatively weak upward
399 motion, heating and drying in the free troposphere, and heating and moistening in the boundary
400 layer. The COS case occurred in strong mid-level easterlies. It was characterized as a squall line
401 with deep strong profiles of upward motion, heating and drying. The BOS case mainly happened
402 in weak mid-level westerlies and descending mid-to-low-level northerlies. It was characterized
403 as widespread, moderate precipitation with embedded convective cells, and lasted much longer
404 than the other two systems. The precipitating stratiform clouds remained at upper levels for
405 several hours evident by upper-level condensational heating and lower-level evaporative cooling.
406 The frequency of LOS cases is similar in both IOPs while the COS and BOS events occur much
407 more often during the wet season than the dry season. The seasonal variation of the diurnal cycle
408 of precipitation, clouds, and environmental variables is mainly due to the COS and BOS events
409 observed in the morning.

410 Previous studies have also shown that the river breeze has an important influence on the
411 diurnal cycle near the Amazon River (e.g. dos Santos et al., 2014; Tanaka et al., 2014; Burleyson
412 et al., 2016) and that the impact of the local circulation can extend as far as 50 km away from the
413 river. This local circulation and the horizontal inhomogeneity of large-scale vertical velocity,
414 heating, and moistening could be better studied using high-resolution 3-D gridded large-scale
415 forcing data from the three-dimensional constrained variational analysis recently developed by
416 Tang and Zhang (2015) and Tang et al. (2016). This will be the subject of a future study.

417

418 *Acknowledgment: The authors gratefully thank Luiz Machado, Jiwen Fan and many others in*
419 *the GoAmazon group for valuable discussions about the synoptic and climate features in*
420 *Amazonia region. This research is supported by the Biological and Environmental Research*
421 *Division in the Office of Sciences of the US Department of Energy (DOE). Work at LLNL was*
422 *supported by the DOE Atmospheric Radiation Measurement (ARM) program and performed*
423 *under the auspices of the U. S. Department of Energy by Lawrence Livermore National*
424 *Laboratory under contract No. DE-AC52-07NA27344. Work at Stony Brook was supported by*
425 *the Office of Science of the U. S. Department of Energy and by the National Science Foundation.*
426 *This manuscript has been authored by employees of Brookhaven Science Associates, LLC with*
427 *support from the ARM program and Atmospheric Systems Research Program under Contract No.*
428 *DE-AC02-98CH10886 with the U.S. Department of Energy. Dr. Zhe Feng at the Pacific*
429 *Northwest National Laboratory (PNNL) is supported by the U.S. DOE, as part of the*
430 *Atmospheric System Research (ASR) Program. PNNL is operated for DOE by Battelle Memorial*
431 *Institute under contract DE-AC05-76RL01830. Work at ECMWF was supported by the U. S.*
432 *Department of Energy via the Atmospheric Systems Research Program under Contract No. DE-*

433 *SC0005259. The satellite analyses are supported by the DOE ARM and ASR Program under*
434 *contract, DE-SC0013896. The publisher by accepting the manuscript for publication*
435 *acknowledges that the United States Government retains a non-exclusive, paid-up, irrevocable,*
436 *world-wide license to publish or reproduce the published form of this manuscript, or allow*
437 *others to do so, for United States Government purposes. We thank The Brazilian National*
438 *Institute of Amazonian Research (INPA), the Amazonas State University (UEA) and Dr. Antonio*
439 *Manzi for providing surface flux data.*

440 **References**

- 441 Ahmed, F., Schumacher, C., Feng, Z., and Hagos, S.: A Retrieval of Tropical Latent Heating
442 Using the 3D Structure of Precipitation Features, *Journal of Applied Meteorology and*
443 *Climatology*, 55, 1965-1982, doi: doi:10.1175/JAMC-D-15-0038.1, 2016.
- 444 Atmospheric Radiation Measurement (ARM) Climate Research Facility, updated hourly.
445 Radiative Flux Analysis (RADFLUX1LONG). 2014-02-15 to 2014-10-10, 3.21297 S 60.5981
446 W: ARM Mobile Facility (MAO) Manacapuru, Amazonas, Brazil; AMF1 (M1). Compiled by C.
447 Long, K. Gaustad and L. Riihimaki. Atmospheric Radiation Measurement (ARM) Climate
448 Research Facility Data Archive: Oak Ridge, Tennessee, USA. Data set accessed 2016-03-09 at
449 doi: 10.5439/1179822, 1994.
- 450 Atmospheric Radiation Measurement (ARM) Climate Research Facility, updated monthly.
451 SCM-Forcing DATA from variational analysis (VARANAL). 2014-02-18 to 2014-10-10,
452 3.21297 S 60.5981 W: ARM Mobile Facility (MAO) Manacapuru, Amazonas, Brazil; AMF1
453 (M1). Compiled by S. Tang, S. Xie and Y. Zhang. Atmospheric Radiation Measurement (ARM)
454 Climate Research Facility Data Archive: Oak Ridge, Tennessee, USA. Data set accessed 2016-
455 07-22 at doi: 10.5439/1273323.
- 456 Atmospheric Radiation Measurement (ARM) Climate Research Facility, updated hourly. Quality
457 Controlled Eddy Correlation Flux Measurement (30QCECOR). 2014-02-15 to 2014-10-10,
458 3.21297 S 60.5981 W: ARM Mobile Facility (MAO) Manacapuru, Amazonas, Brazil; AMF1
459 (M1). Compiled by R. McCoy, Y. Zhang and S. Xie. Atmospheric Radiation Measurement
460 (ARM) Climate Research Facility Data Archive: Oak Ridge, Tennessee, USA. Data set accessed
461 2016-03-22 at doi: 10.5439/1097546, 2003.
- 462 Burleyson, C. D., Feng, Z., Hagos, S., Fast, J., Machado, L. A. T., and Martin, S. T.: Spatial
463 variability of the background diurnal cycle of deep convection around the GoAmazon2014/5
464 field campaign sites, *Journal of Applied Meteorology and Climatology*, in revision, doi, 2016.
- 465 Cifelli, R., Petersen, W. A., Carey, L. D., Rutledge, S. A., and da Silva Dias, M. A. F.: Radar
466 observations of the kinematic, microphysical, and precipitation characteristics of two MCSs in
467 TRMM LBA, *Journal of Geophysical Research: Atmospheres*, 107, LBA 44-41-LBA 44-16, doi:
468 10.1029/2000JD000264, 2002.
- 469 Cressman, G. P.: AN OPERATIONAL OBJECTIVE ANALYSIS SYSTEM, *Monthly Weather*
470 *Review*, 87, 367-374, doi: doi:10.1175/1520-0493(1959)087<0367:AOOAS>2.0.CO;2, 1959.
- 471 Cutrim, E. M. C., Martin, D. W., Butzow, D. G., Silva, I. M., and Yulaeva, E.: Pilot Analysis of
472 Hourly Rainfall in Central and Eastern Amazonia, *Journal of Climate*, 13, 1326-1334, doi:
473 10.1175/1520-0442(2000)013<1326:PAOHRI>2.0.CO;2, 2000.

474 Dee, D. P., Uppala, S. M., Simmons, A. J., Berrisford, P., Poli, P., Kobayashi, S., Andrae, U.,
475 Balmaseda, M. A., Balsamo, G., Bauer, P., Bechtold, P., Beljaars, A. C. M., van de Berg, L.,
476 Bidlot, J., Bormann, N., Delsol, C., Dragani, R., Fuentes, M., Geer, A. J., Haimberger, L., Healy,
477 S. B., Hersbach, H., Hólm, E. V., Isaksen, L., Kållberg, P., Köhler, M., Matricardi, M., McNally,
478 A. P., Monge-Sanz, B. M., Morcrette, J. J., Park, B. K., Peubey, C., de Rosnay, P., Tavolato, C.,
479 Thépaut, J. N., and Vitart, F.: The ERA-Interim reanalysis: configuration and performance of the
480 data assimilation system, *Quarterly Journal of the Royal Meteorological Society*, 137, 553-597,
481 doi: 10.1002/qj.828, 2011.

482 dos Santos, M. J., Silva Dias, M. A. F., and Freitas, E. D.: Influence of local circulations on wind,
483 moisture, and precipitation close to Manaus City, Amazon Region, Brazil, *Journal of*
484 *Geophysical Research: Atmospheres*, 119, 13,233-213,249, doi: 10.1002/2014JD021969, 2014.

485 Feng, Z., McFarlane, S. A., Schumacher, C., Ellis, S., Comstock, J., and Bharadwaj, N.:
486 Constructing a Merged Cloud-Precipitation Radar Dataset for Tropical Convective Clouds
487 during the DYNAMO/AMIE Experiment at Addu Atoll, *J. Atmos. Oceanic Technol.*, 31, 1021-
488 1042, doi: 10.1175/JTECH-D-13-00132.1, 2014.

489 Filho, A. J. P., Carbone, R. E., Tuttle, J. D., and Karam, H. A.: Convective Rainfall in Amazonia
490 and Adjacent Tropics, *Atmospheric and Climate Sciences*, 5, 137-161, doi:
491 10.4236/acs.2015.52011, 2015.

492 Fu, R., Zhu, B., and Dickinson, R. E.: How Do Atmosphere and Land Surface Influence
493 Seasonal Changes of Convection in the Tropical Amazon?, *Journal of Climate*, 12, 1306-1321,
494 doi: doi:10.1175/1520-0442(1999)012<1306:HDAALS>2.0.CO;2, 1999.

495 Fu, R., Dickinson, R. E., Chen, M., and Wang, H.: How Do Tropical Sea Surface Temperatures
496 Influence the Seasonal Distribution of Precipitation in the Equatorial Amazon?, *Journal of*
497 *Climate*, 14, 4003-4026, doi: doi:10.1175/1520-0442(2001)014<4003:HDTSSST>2.0.CO;2, 2001.

498 Giangrande, S., Toto, T., Jensen, M. P., Bartholomew, M., Feng, Z., Protat, A., Williams, C.,
499 Schumacher, C., and Machado, L.: Convective Cloud Vertical Velocity and Mass-Flux
500 Characteristics from Radar Wind Profiler Observations During GoAmazon2014/5, *Journal of*
501 *Geophysical Research: Atmospheres*, in review, doi, 2016.

502 Greco, S., Swap, R., Garstang, M., Ulanski, S., Shipham, M., Harriss, R. C., Talbot, R., Andreae,
503 M. O., and Artaxo, P.: Rainfall and surface kinematic conditions over central Amazonia during
504 ABLE 2B, *Journal of Geophysical Research: Atmospheres*, 95, 17001-17014, doi:
505 10.1029/JD095iD10p17001, 1990.

506 Greco, S., Scala, J., Halverson, J., Jr., H. L. M., Tao, W.-K., and Garstang, M.: Amazon Coastal
507 Squall Lines. Part II: Heat and Moisture Transports, *Monthly Weather Review*, 122, 623-635,
508 doi: doi:10.1175/1520-0493(1994)122<0623:ACSLPI>2.0.CO;2, 1994.

509 Hack, J. J., and Schubert, W. H.: Some dynamical properties of idealized thermally-forced
510 meridional circulations in the tropics, *Meteorol. Atmos. Phys.*, 44, 101-117, doi:
511 10.1007/BF01026813, 1990.

512 Harriss, R. C., Wofsy, S. C., Garstang, M., Browell, E. V., Molion, L. C. B., McNeal, R. J.,
513 Hoell, J. M., Bendura, R. J., Beck, S. M., Navarro, R. L., Riley, J. T., and Snell, R. L.: The
514 Amazon Boundary Layer Experiment (ABLE 2A): dry season 1985, *Journal of Geophysical*
515 *Research: Atmospheres*, 93, 1351-1360, doi: 10.1029/JD093iD02p01351, 1988.

516 Harriss, R. C., Garstang, M., Wofsy, S. C., Beck, S. M., Bendura, R. J., Coelho, J. R. B., Drewry,
517 J. W., Hoell, J. M., Matson, P. A., McNeal, R. J., Molion, L. C. B., Navarro, R. L., Rabine, V.,
518 and Snell, R. L.: The Amazon Boundary Layer Experiment: Wet season 1987, *Journal of*
519 *Geophysical Research: Atmospheres*, 95, 16721-16736, doi: 10.1029/JD095iD10p16721, 1990.

520 Hartmann, D. L., Hendon, H. H., and Houze, R. A.: Some Implications of the Mesoscale
521 Circulations in Tropical Cloud Clusters for Large-Scale Dynamics and Climate, *Journal of the*
522 *Atmospheric Sciences*, 41, 113-121, doi: 10.1175/1520-
523 0469(1984)041<0113:SIOTMC>2.0.CO;2, 1984.

524 Janowiak, J. E., Kousky, V. E., and Joyce, R. J.: Diurnal cycle of precipitation determined from
525 the CMORPH high spatial and temporal resolution global precipitation analyses, *Journal of*
526 *Geophysical Research: Atmospheres*, 110, n/a-n/a, doi: 10.1029/2005JD006156, 2005.

527 Johnson, R. H.: Partitioning Tropical Heat and Moisture Budgets into Cumulus and Mesoscale
528 Components: Implications for Cumulus Parameterization, *Monthly Weather Review*, 112, 1590-
529 1601, doi: 10.1175/1520-0493(1984)112<1590:PTHAMB>2.0.CO;2, 1984.

530 Johnson, R. H., and Lin, X.: Episodic Trade Wind Regimes over the Western Pacific Warm Pool,
531 *Journal of the Atmospheric Sciences*, 54, 2020-2034, doi: 10.1175/1520-
532 0469(1997)054<2020:ETWROT>2.0.CO;2, 1997.

533 Johnson, R. H., Ciesielski, P. E., and Rickenbach, T. M.: A Further Look at Q1 and Q2 from
534 TOGA COARE, *Meteorological Monographs*, 56, 1.1-1.12, doi:
535 doi:10.1175/AMSMONOGRAPHS-D-15-0002.1, 2016.

536 Khaiyer, M., Minnis, P., Doelling, D. R., Nordeen, M. L., Palikonda, R., Rutan, D. A., and Yi, Y.:
537 Improved TOA broadband shortwave and longwave fluxes derived from satellites over the
538 Tropical Western Pacific, 13th Conference on Atmospheric Radiation, *Am. Meteorol. Soc.*,
539 Portland, OR. 27 June to 2 July, 2010.

540 Kollias, P., Miller, M. A., Luke, E. P., Johnson, K. L., Clothiaux, E. E., Moran, K. P., Widener,
541 K. B., and Albrecht, B. A.: The Atmospheric Radiation Measurement Program Cloud Profiling
542 Radars: Second-Generation Sampling Strategies, Processing, and Cloud Data Products, *Journal*
543 *of Atmospheric and Oceanic Technology*, 24, 1199-1214, doi: 10.1175/JTECH2033.1, 2007.

544 Lau, K. M., and Peng, L.: Origin of Low-Frequency (Intraseasonal) Oscillations in the Tropical
545 Atmosphere. Part I: Basic Theory, *Journal of the Atmospheric Sciences*, 44, 950-972, doi:
546 10.1175/1520-0469(1987)044<0950:OOLFOI>2.0.CO;2, 1987.

547 Li, W., Fu, R., and Dickinson, R. E.: Rainfall and its seasonality over the Amazon in the 21st
548 century as assessed by the coupled models for the IPCC AR4, *Journal of Geophysical Research:*
549 *Atmospheres*, 111, n/a-n/a, doi: 10.1029/2005JD006355, 2006.

550 Lin, X., and Johnson, R. H.: Heating, Moistening, and Rainfall over the Western Pacific Warm
551 Pool during TOGA COARE, *Journal of the Atmospheric Sciences*, 53, 3367-3383, doi:
552 10.1175/1520-0469(1996)053<3367:HMAROT>2.0.CO;2, 1996.

553 Machado, L. A. T., Laurent, H., Dessay, N., and Miranda, I.: Seasonal and diurnal variability of
554 convection over the Amazonia: A comparison of different vegetation types and large scale
555 forcing, *Theor Appl Climatol*, 78, 61-77, doi: 10.1007/s00704-004-0044-9, 2004.

556 Machado, L. A. T., Silva Dias, M. A. F., Morales, C., Fisch, G., Vila, D., Albrecht, R., Goodman,
557 S. J., Calheiros, A. J. P., Biscaro, T., Kummerow, C., Cohen, J., Fitzjarrald, D., Nascimento, E.
558 L., Sakamoto, M. S., Cunningham, C., Chaboureau, J.-P., Petersen, W. A., Adams, D. K.,
559 Baldini, L., Angelis, C. F., Sapucci, L. F., Salio, P., Barbosa, H. M. J., Landulfo, E., Souza, R. A.
560 F., Blakeslee, R. J., Bailey, J., Freitas, S., Lima, W. F. A., and Tokay, A.: The Chuva Project:
561 How Does Convection Vary across Brazil?, *Bulletin of the American Meteorological Society*, 95,
562 1365-1380, doi: 10.1175/BAMS-D-13-00084.1, 2014.

563 Marengo, J. A., Liebmann, B., Grimm, A. M., Misra, V., Silva Dias, P. L., Cavalcanti, I. F. A.,
564 Carvalho, L. M. V., Berbery, E. H., Ambrizzi, T., Vera, C. S., Saulo, A. C., Noguez-Paegle, J.,
565 Zipser, E., Seth, A., and Alves, L. M.: Recent developments on the South American monsoon
566 system, *International Journal of Climatology*, 32, 1-21, doi: 10.1002/joc.2254, 2012.

567 Martin, S. T., Artaxo, P., Machado, L. A. T., Manzi, A. O., Souza, R. A. F., Schumacher, C.,
568 Wang, J., Andreae, M. O., Barbosa, H. M. J., Fan, J., Fisch, G., Goldstein, A. H., Guenther, A.,
569 Jimenez, J. L., Pöschl, U., Silva Dias, M. A., Smith, J. N., and Wendisch, M.: Introduction:
570 Observations and Modeling of the Green Ocean Amazon (GoAmazon2014/5), *Atmos. Chem.*
571 *Phys.*, 16, 4785-4797, doi: 10.5194/acp-16-4785-2016, 2016.

572 Minnis, P., and Harrison, E. F.: Diurnal Variability of Regional Cloud and Clear-Sky Radiative
573 Parameters Derived from GOES Data. Part II: November 1978 Cloud Distributions, *Journal of*
574 *Climate and Applied Meteorology*, 23, 1012-1031, doi: doi:10.1175/1520-
575 0450(1984)023<1012:DVORCA>2.0.CO;2, 1984.

576 Minnis, P., and Smith, W. L.: Cloud and radiative fields derived from GOES-8 during SUCCESS
577 and the ARM-UAV spring 1996 flight series, *Geophysical Research Letters*, 25, 1113-1116, doi:
578 10.1029/98GL00301, 1998.

579 Neale, R. B., Chen, C.-C., Gettelman, A., Lauritzen, P. H., Park, S., Williamson, D., Conley, A.,
580 Garcia, R., Kinnison, D., Lamarque, J., Marsh, D., Mills, M., Smith, A., Tilmes, S., Vitt, F.,
581 Morrison, H., Cameron-Smith, P., Collins, W. D., Iacono, M., Easter, R., Ghan, S. J., Liu, X.,
582 Rasch, P. J., and Taylor, M. A.: Description of the NCAR Community Atmosphere Model
583 (CAM 5.0), NCAR Technical Note NCARTN-4861STR, 274, 2012.

584 Nitta, T., and Esbensen, S.: Heat and Moisture Budget Analyses Using BOMEX Data, Monthly
585 Weather Review, 102, 17-28, doi: 10.1175/1520-0493(1974)102<0017:HAMBAU>2.0.CO;2,
586 1974.

587 Nobre, C. A., Obregón, G. O., Marengo, J. A., Fu, R., and Poveda, G.: Characteristics of
588 Amazonian Climate: Main Features, in: Amazonia and Global Change, American Geophysical
589 Union, 149-162, 2009.

590 Puri, K.: Some Experiments on the Use of Tropical Diabatic Heating Information for Initial State
591 Specification, Monthly Weather Review, 115, 1394-1406, doi: 10.1175/1520-
592 0493(1987)115<1394:SEOTUO>2.0.CO;2, 1987.

593 Schumacher, C., and Houze, R. A.: Stratiform Rain in the Tropics as Seen by the TRMM
594 Precipitation Radar*, Journal of Climate, 16, 1739-1756, doi: 10.1175/1520-
595 0442(2003)016<1739:SRITTA>2.0.CO;2, 2003.

596 Schumacher, C., Zhang, M. H., and Ciesielski, P. E.: Heating Structures of the TRMM Field
597 Campaigns, Journal of the Atmospheric Sciences, 64, 2593-2610, doi: 10.1175/JAS3938.1, 2007.

598 Schumacher, C., Ciesielski, P. E., and Zhang, M. H.: Tropical Cloud Heating Profiles: Analysis
599 from KWAJEX, Monthly Weather Review, 136, 4289-4300, doi: 10.1175/2008MWR2275.1,
600 2008.

601 Silva Dias, M. A. F., Petersen, W., Silva Dias, P. L., Cifelli, R., Betts, A. K., Longo, M., Gomes,
602 A. M., Fisch, G. F., Lima, M. A., Antonio, M. A., and Albrecht, R. I.: A case study of convective
603 organization into precipitating lines in the Southwest Amazon during the WETAMC and
604 TRMM-LBA, Journal of Geophysical Research: Atmospheres, 107, LBA 46-41-LBA 46-23, doi:
605 10.1029/2001JD000375, 2002a.

606 Silva Dias, M. A. F., Rutledge, S., Kabat, P., Silva Dias, P. L., Nobre, C., Fisch, G., Dolman, A.
607 J., Zipser, E., Garstang, M., Manzi, A. O., Fuentes, J. D., Rocha, H. R., Marengo, J., Plana-
608 Fattori, A., Sá, L. D. A., Alvalá, R. C. S., Andreae, M. O., Artaxo, P., Gielow, R., and Gatti, L.:
609 Cloud and rain processes in a biosphere-atmosphere interaction context in the Amazon Region,
610 Journal of Geophysical Research: Atmospheres, 107, LBA 39-31-LBA 39-18, doi:
611 10.1029/2001JD000335, 2002b.

612 Tanaka, L. M. d. S., Satyamurty, P., and Machado, L. A. T.: Diurnal variation of precipitation in
613 central Amazon Basin, *International Journal of Climatology*, 34, 3574-3584, doi:
614 10.1002/joc.3929, 2014.

615 Tang, S., and Zhang, M.: Three-dimensional constrained variational analysis: Approach and
616 application to analysis of atmospheric diabatic heating and derivative fields during an ARM SGP
617 intensive observational period, *Journal of Geophysical Research: Atmospheres*, 120, 7283-7299,
618 doi: 10.1002/2015JD023621, 2015.

619 Tang, S., Zhang, M., and Xie, S.: An ensemble constrained variational analysis of atmospheric
620 forcing data and its application to evaluate clouds in CAM5, *Journal of Geophysical Research:*
621 *Atmospheres*, 121, 33-48, doi: 10.1002/2015JD024167, 2016.

622 Williams, E., Rosenfeld, D., Madden, N., Gerlach, J., Gears, N., Atkinson, L., Dunnemann, N.,
623 Frostrom, G., Antonio, M., Biazon, B., Camargo, R., Franca, H., Gomes, A., Lima, M., Machado,
624 R., Manhaes, S., Nachtigall, L., Piva, H., Quintiliano, W., Machado, L., Artaxo, P., Roberts, G.,
625 Renno, N., Blakeslee, R., Bailey, J., Boccippio, D., Betts, A., Wolff, D., Roy, B., Halverson, J.,
626 Rickenbach, T., Fuentes, J., and Avelino, E.: Contrasting convective regimes over the Amazon:
627 Implications for cloud electrification, *Journal of Geophysical Research: Atmospheres*, 107, LBA
628 50-51-LBA 50-19, doi: 10.1029/2001JD000380, 2002.

629 Xie, S., Cederwall, R. T., and Zhang, M.: Developing long-term single-column model/cloud
630 system-resolving model forcing data using numerical weather prediction products constrained by
631 surface and top of the atmosphere observations, *Journal of Geophysical Research*, 109, doi:
632 10.1029/2003jd004045, 2004.

633 Xie, S., Hume, T., Jakob, C., Klein, S. A., McCoy, R. B., and Zhang, M.: Observed Large-Scale
634 Structures and Diabatic Heating and Drying Profiles during TWP-ICE, *Journal of Climate*, 23,
635 57-79, doi: 10.1175/2009jcli3071.1, 2010a.

636 Xie, S., McCoy, R. B., Klein, S. A., Cederwall, R. T., Wiscombe, W. J., Jensen, M. P., Johnson,
637 K. L., Clothiaux, E. E., Gaustad, K. L., Long, C. N., Mather, J. H., McFarlane, S. A., Shi, Y.,
638 Golaz, J.-C., Lin, Y., Hall, S. D., McCord, R. A., Palanisamy, G., and Turner, D. D.: CLOUDS
639 AND MORE: ARM Climate Modeling Best Estimate Data, *Bulletin of the American*
640 *Meteorological Society*, 91, 13-20, doi: 10.1175/2009BAMS2891.1, 2010b.

641 Yanai, M., Esbensen, S., and Chu, J.-H.: Determination of Bulk Properties of Tropical Cloud
642 Clusters from Large-Scale Heat and Moisture Budgets, *Journal of the Atmospheric Sciences*, 30,
643 611-627, doi: 10.1175/1520-0469(1973)030<0611:DOBPOT>2.0.CO;2, 1973.

644 Zhang, M., and Lin, J.: Constrained Variational Analysis of Sounding Data Based on Column-
645 Integrated Budgets of Mass, Heat, Moisture, and Momentum: Approach and Application to

646 ARM Measurements, *Journal of the Atmospheric Sciences*, 54, 1503-1524, doi: 10.1175/1520-
647 0469(1997)054<1503:CVAOSD>2.0.CO;2, 1997.

648 Zhang, M., Lin, J., Cederwall, R. T., Yio, J. J., and Xie, S. C.: Objective Analysis of ARM IOP
649 Data: Method and Sensitivity, *Monthly Weather Review*, 129, 295-311, doi: 10.1175/1520-
650 0493(2001)129<0295:OAOAID>2.0.CO;2, 2001.

651

652
653
654
655
656
657
658
659
660
661
662
663
664
665
666
667
668
669
670
671
672
673
674
675
676
677
678
679
680
681
682
683

Figure and Table Captions:

Table 1: number of convective systems identified in the morning and afternoon during IOP1 and IOP2.

Figure 1: The location of GoAmazon site in this study. The red octagon represents the analysis domain. Locations of observational sites are indicated by yellow pentagrams. Locations of cities are indicated by white dots.

Figure 2: The sea-level pressure (shaded) and 10-meter horizontal wind (vector) averaged for IOP1 (left) and IOP2 (right). The pentagram indicates the location of GoAmazon site.

Figure 3: Domain averaged time series of (from top to bottom) horizontal (u) wind, meridional (v) wind, relative humidity, cloud frequency (point observation at the ARM site) and precipitation for IOP1 (left) and IOP2 (right). The blank areas in cloud frequency indicate missing data. The three straight black lines in IOP1 show the three cases chosen in section 6.

Figure 4: The time series (top) and temporal mean profiles (bottom) of large-scale vertical velocity for IOP1 (left) and IOP2 (right).

Figure 5: The time series (top) and temporal mean profiles (bottom) of apparent heating source Q_1 for IOP1 (left) and IOP2 (right).

Figure 6: The time series (top) and temporal mean profiles (bottom) of apparent moisture sink Q_2 for IOP1 (left) and IOP2 (right).

Figure 7: The diurnal cycle of precipitation (up) and CAPE and CIN (bottom) for both IOPs.

Figure 8: The diurnal cycle of (from top to bottom) cloud frequency, large-scale vertical velocity, Q_1 , Q_2 and $Q_1 - Q_2 - Q_{rad}$ for IOP1 and IOP2. The black lines are zero-lines.

Figure 9: SIPAM radar reflectivity snapshots (left) and time series of domain-mean precipitation (right) for three cases of precipitating systems. From top to bottom: LOS, COS and BOS. The black octagons indicate the GoAmazon domain, and the red arrows indicate the propagating direction of the system.

Figure 10: The time series of (a) cloud frequency, (b) relative humidity, (c) surface CAPE and CIN, (d) u wind, (e) v wind, (f) vertical velocity, (g) Q_1 , (h) Q_2 and (i) $Q_1 - Q_2 - Q_{rad}$ for the LOS case. The black lines are zero-lines. The shaded and white areas in (b) indicate nighttime and daytime.

Figure 11: Similar as Figure 10 but for the COS case.

Figure 12: Similar as Figure 10 but for the BOS case.

	IOP1		IOP2	
	Morning	Afternoon	Morning	Afternoon
Locally Occurring Systems (LOS)	0	19	0	16
Coastal Occurring Systems (COS)	8	2	0	1
Basin Occurring Systems (BOS)	8	1	3	2

684

685 Table 1: number of convective systems identified in the morning and afternoon during IOP1 and
686 IOP2.

687

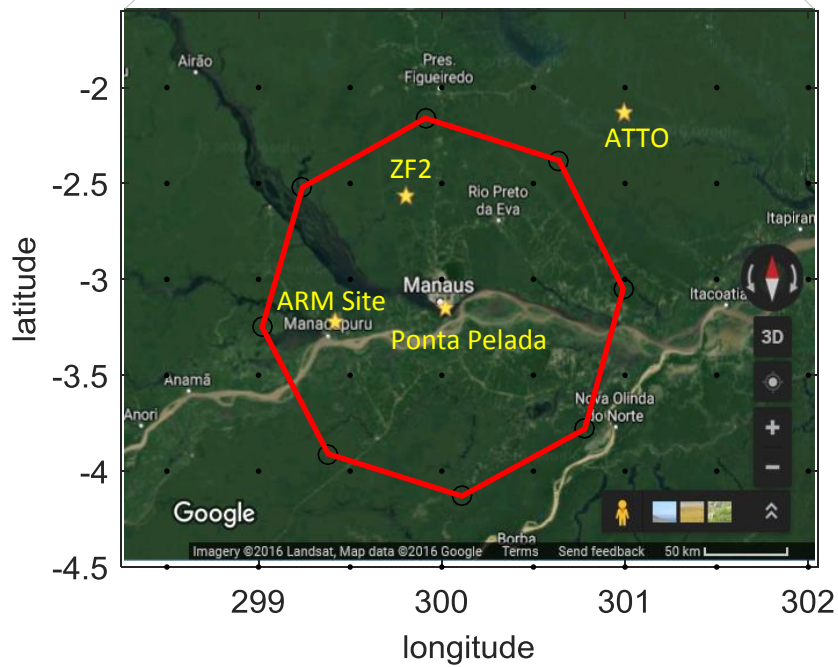
688

689

690

691

692



693

694 Figure 1: The location of GoAmazon site (top) and the analysis domain for this study (bottom).
695 Locations of measurement sites are indicated by yellow pentagrams. Locations of cities are indicated by
696 white dots.

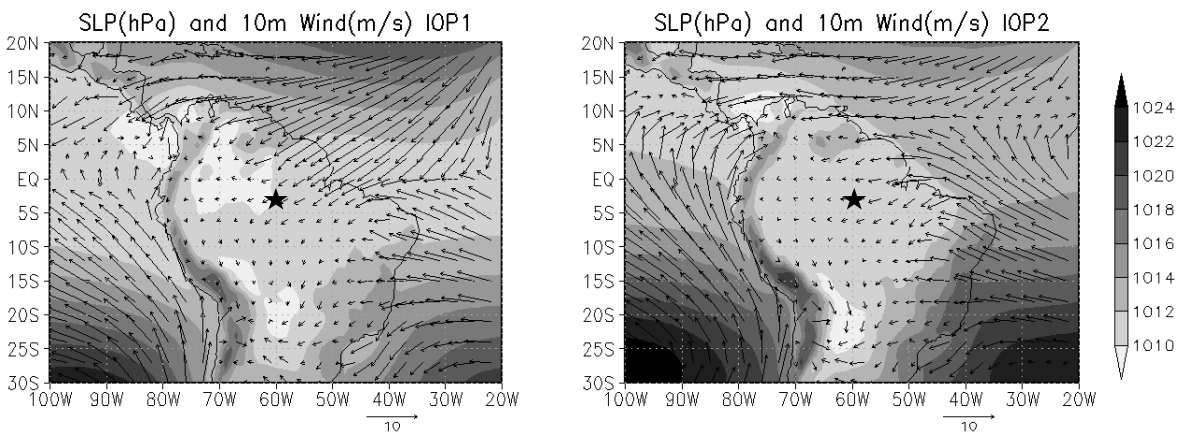
697

698

699

700

701



702

703 Figure 2: The sea-level pressure (shaded) and 10-meter horizontal wind (vector) averaged for IOP1 (left)
704 and IOP2 (right). The pentagram indicates the location of GoAmazon site.

705

706

707

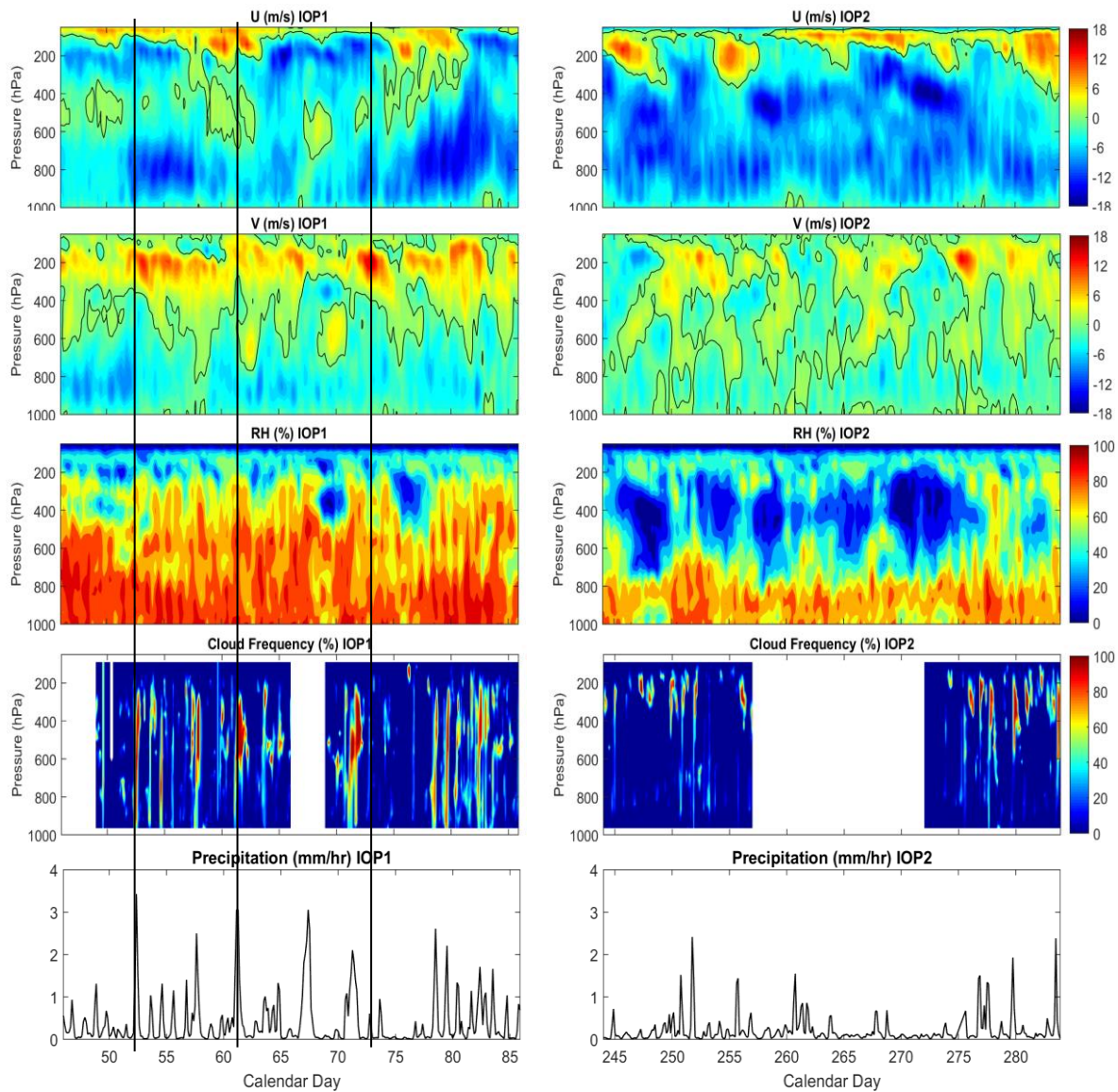
708

709

710

711

712



713

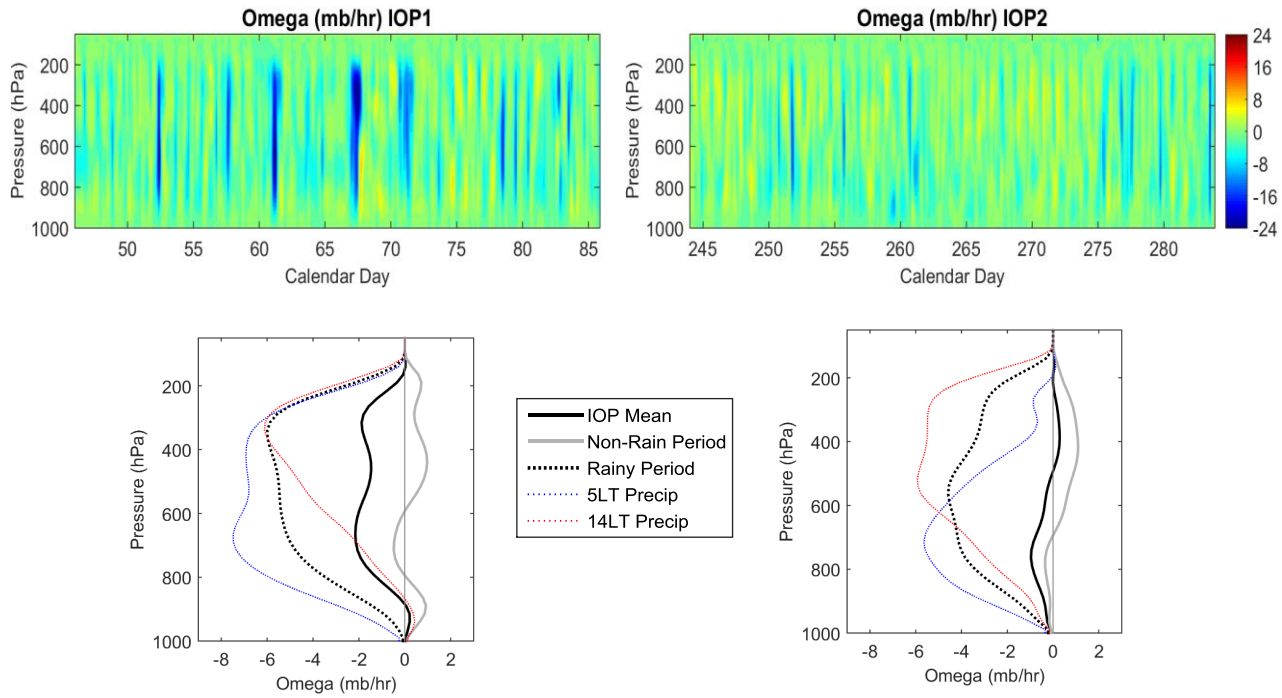
714 Figure 3: Domain averaged time series of (from top to bottom) horizontal (u) wind, meridional (v) wind,
715 relative humidity, cloud frequency (point observation at the ARM site) and precipitation for IOP1 (left)
716 and IOP2 (right). The blank areas in cloud frequency indicate missing data. The three straight black lines
717 in IOP1 show the three cases chosen in section 6.

718

719

720

721



722

723

724

725 Figure 4: The time series (top) and temporal mean profiles (bottom) of large-scale vertical velocity for
726 IOP1 (left) and IOP2 (right).

727

728

729

730

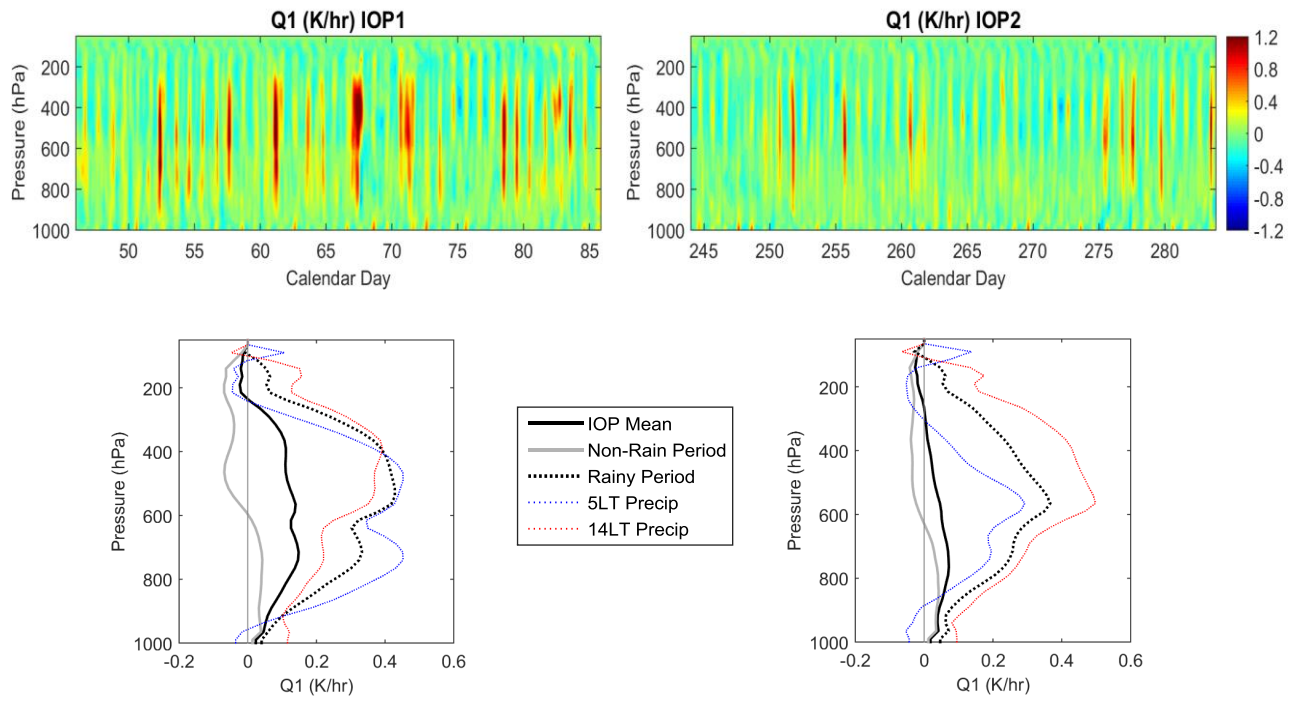
731

732

733

734

735



736

737

738

739 Figure 5: The time series (top) and temporal mean profiles (bottom) of apparent heating source Q_1 for
740 IOP1 (left) and IOP2 (right).

741

742

743

744

745

746

747

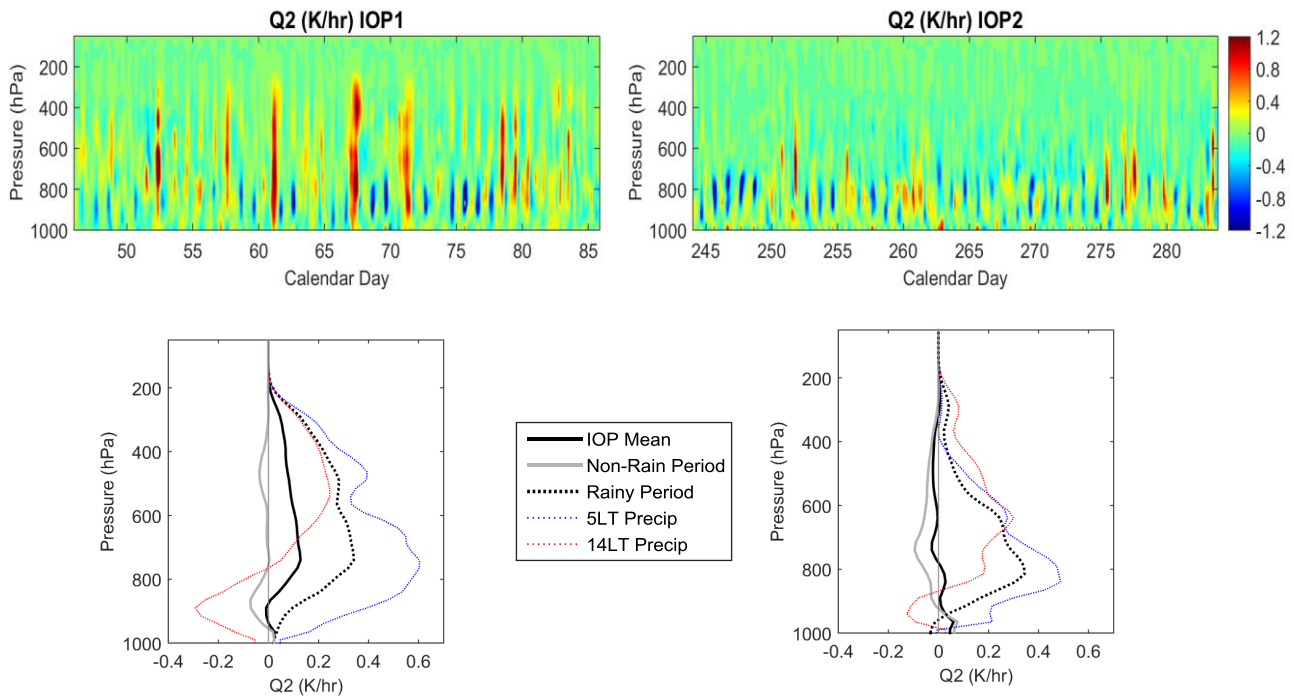
748

749

750

751

752



753

754 Figure 6: The time series (top) and temporal mean profiles (bottom) of apparent moisture sink Q_2 for
755 IOP1 (left) and IOP2 (right).

756

757

758

759

760

761

762

763

764

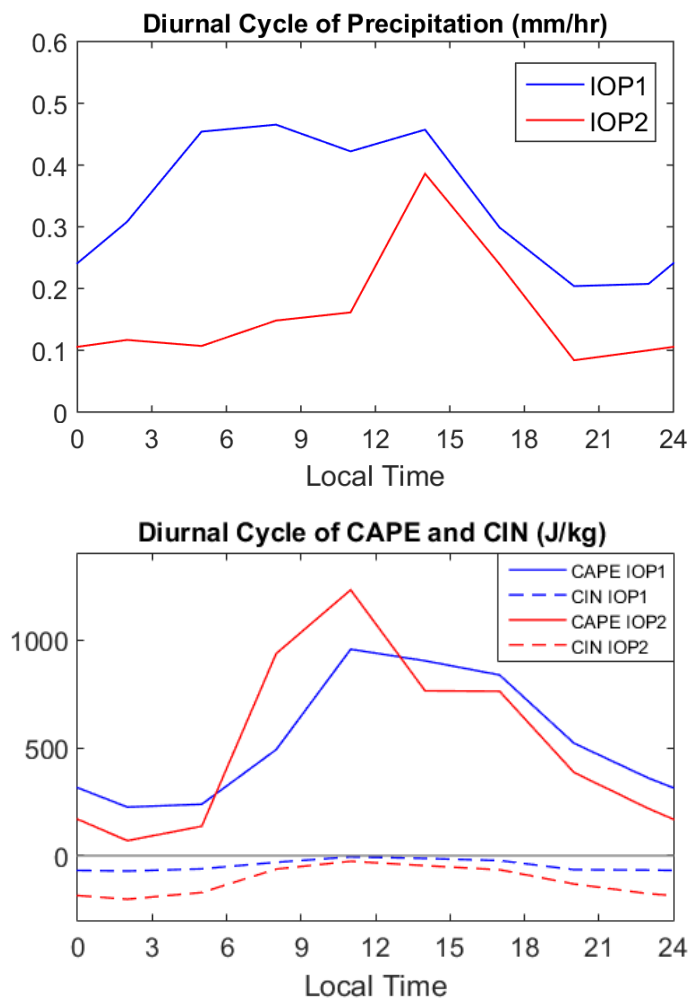
765

766

767

768

769



770

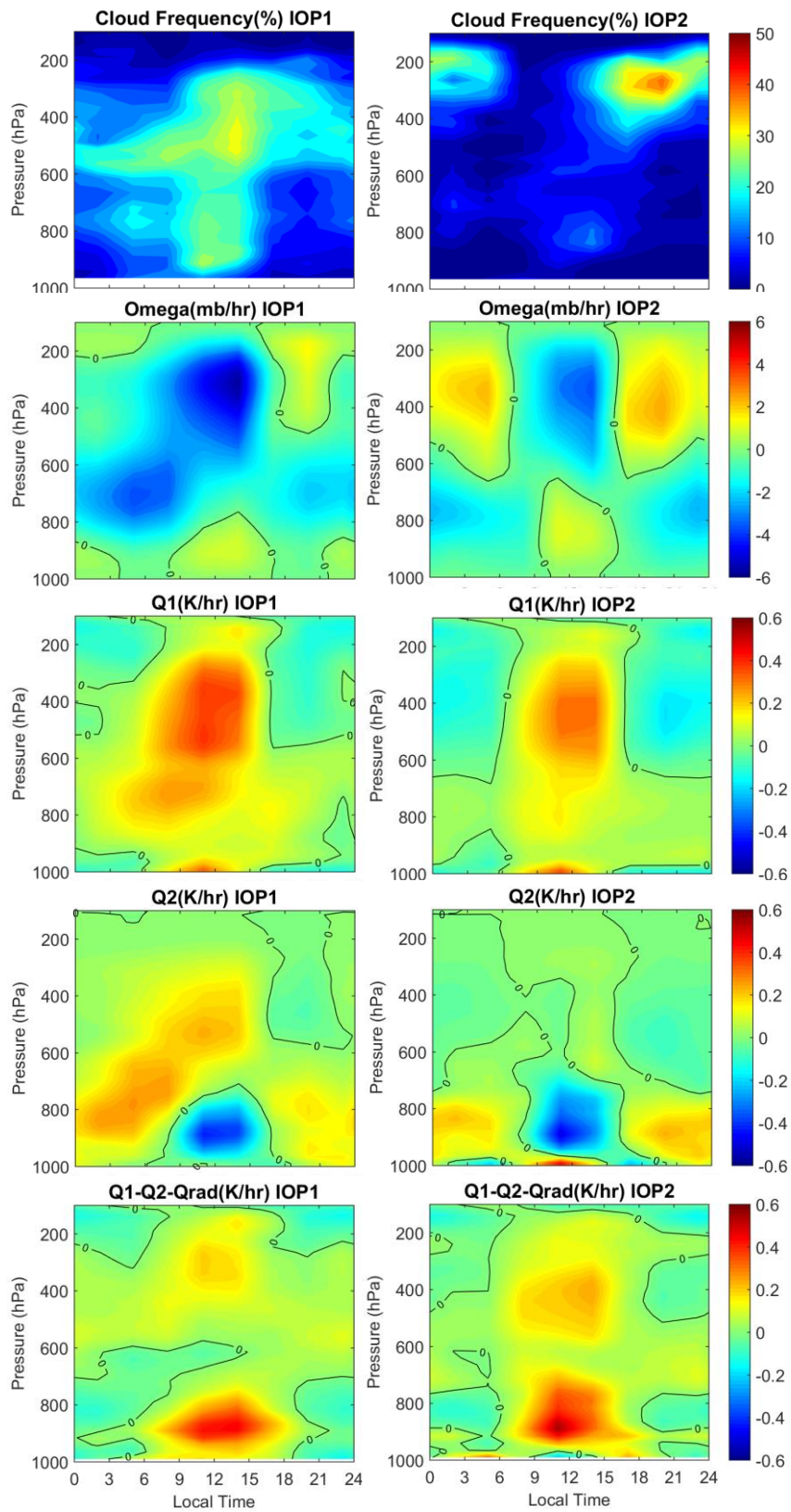
771 Figure 7: The diurnal cycle of precipitation (up) and CAPE and CIN (bottom) for both IOPs.

772

773

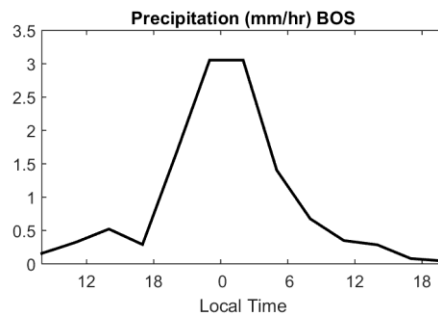
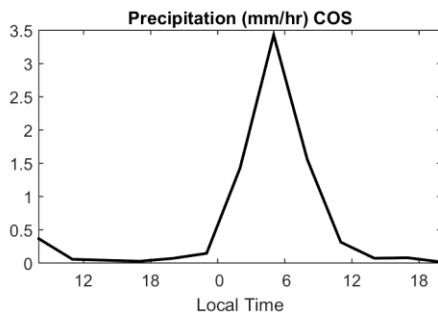
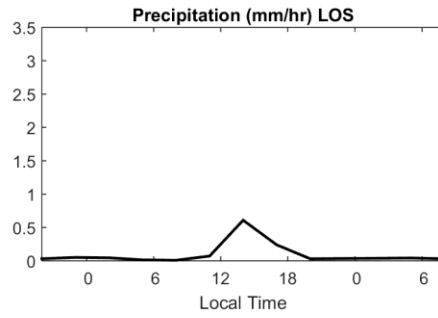
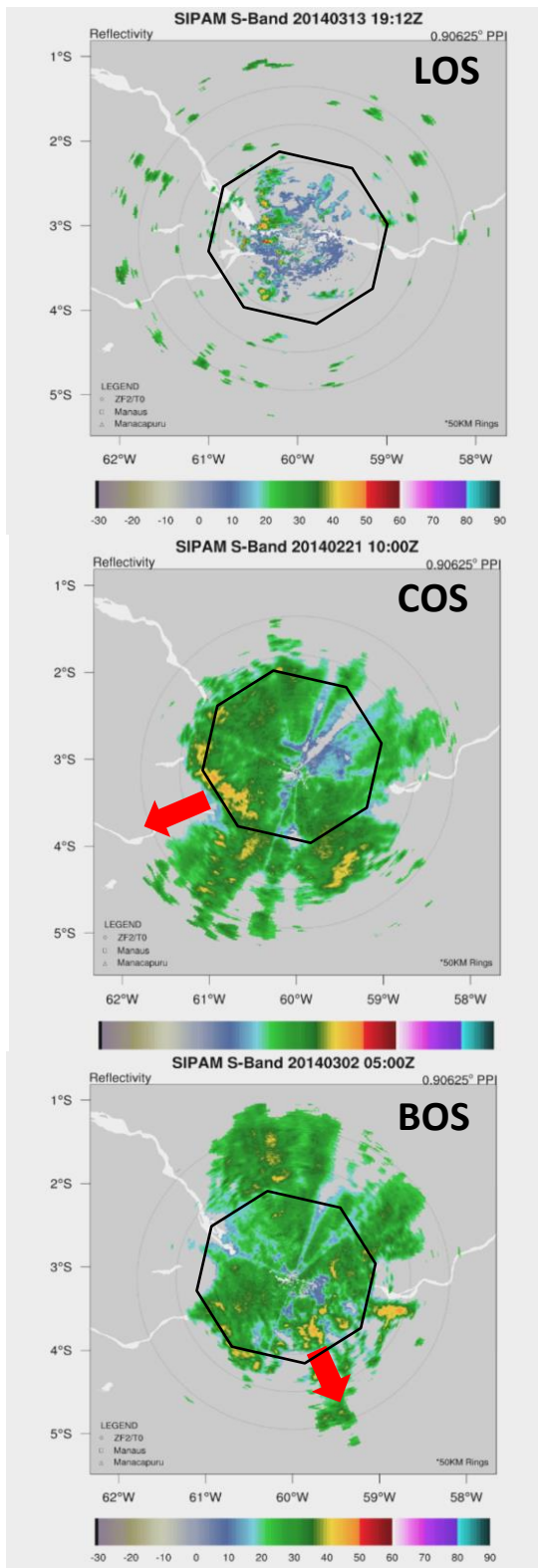
774

775



776

777 Figure 8: The diurnal cycle of (from top to bottom) cloud frequency, large-scale vertical velocity, Q_1 , Q_2
 778 and $Q_1 - Q_2 - Q_{rad}$ for IOP1 and IOP2. The black lines are zero-lines.

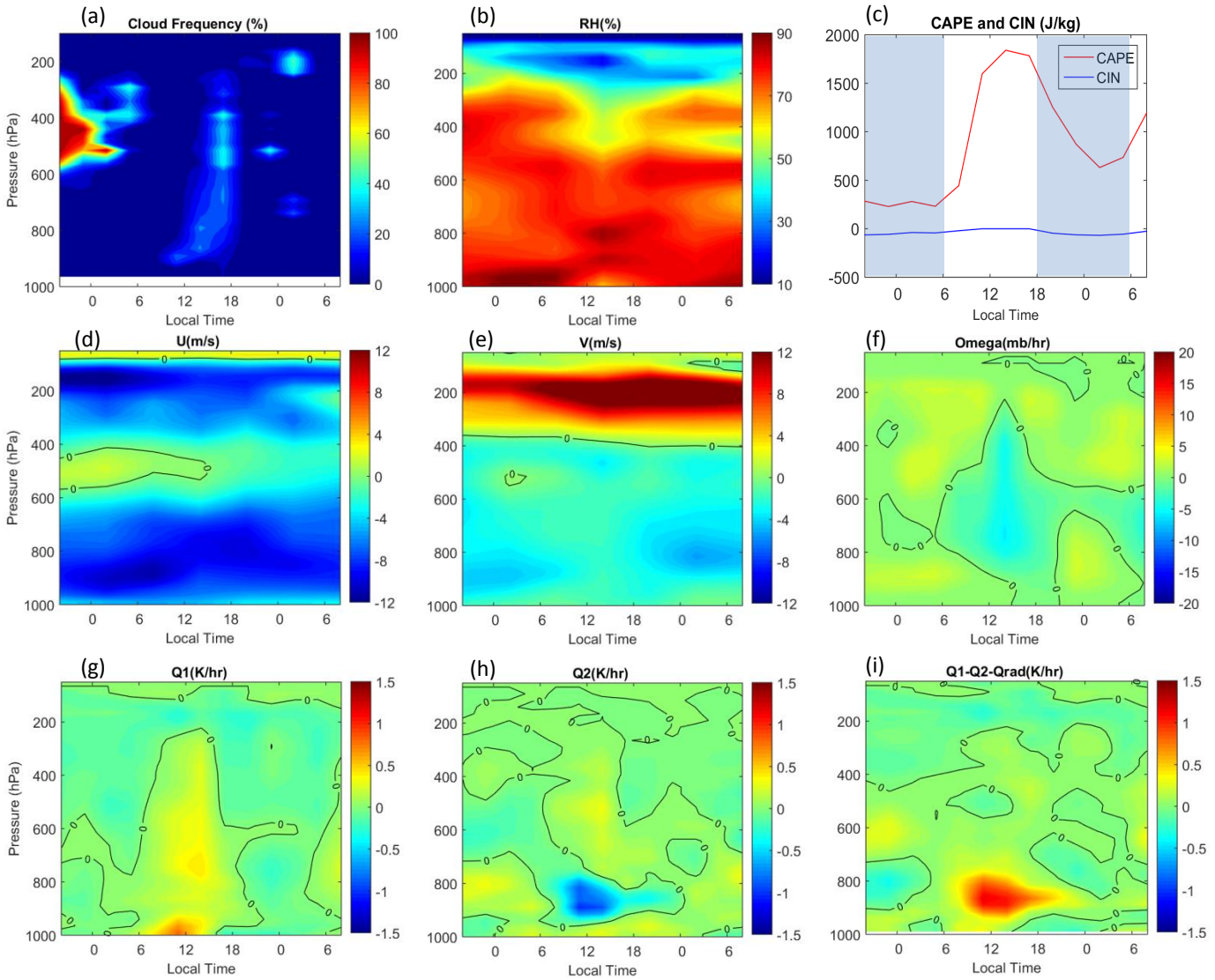


779

780 Figure 9: SIPAM radar reflectivity snapshots (left) and time series of domain-mean precipitation (right)
 781 for three cases of precipitating systems. From top to bottom: LOS, COS and BOS. The black octagons
 782 indicate the GoAmazon domain, and the red arrows indicate the propagating direction of the system.

783

LOS (14 March 2014)

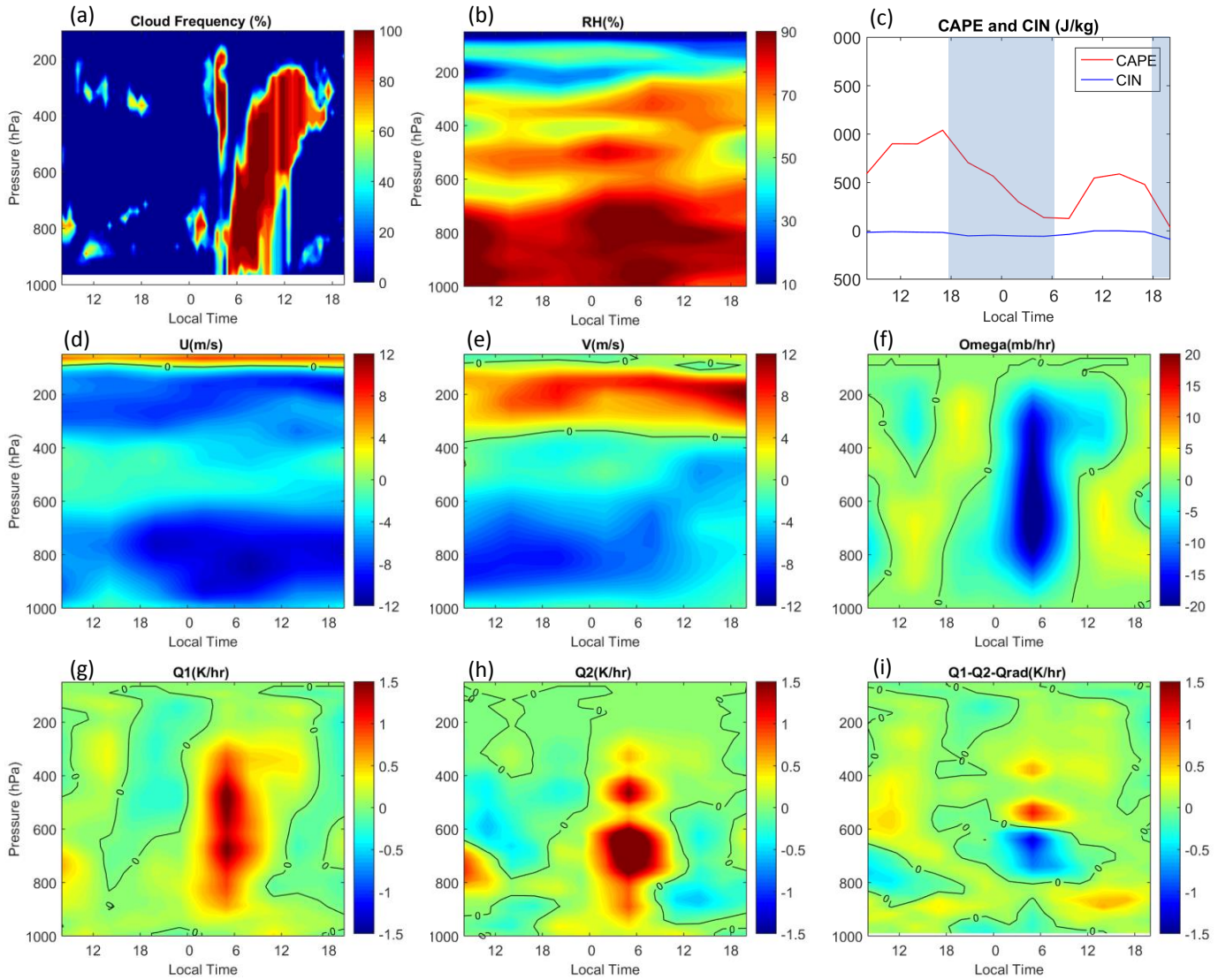


784

785 Figure 10: The time series of (a) cloud frequency, (b) relative humidity, (c) surface CAPE and CIN, (d) u
 786 wind, (e) v wind, (f) vertical velocity, (g) Q_1 , (h) Q_2 and (i) $Q_1 - Q_2 - Q_{rad}$ for the LOS case. The black
 787 lines are zero-lines. The shaded and white areas in (c) indicate nighttime and daytime.

788

COS (20 – 21 February 2014)



790

791 Figure 11: Similar as Figure 10 but for the COS case.

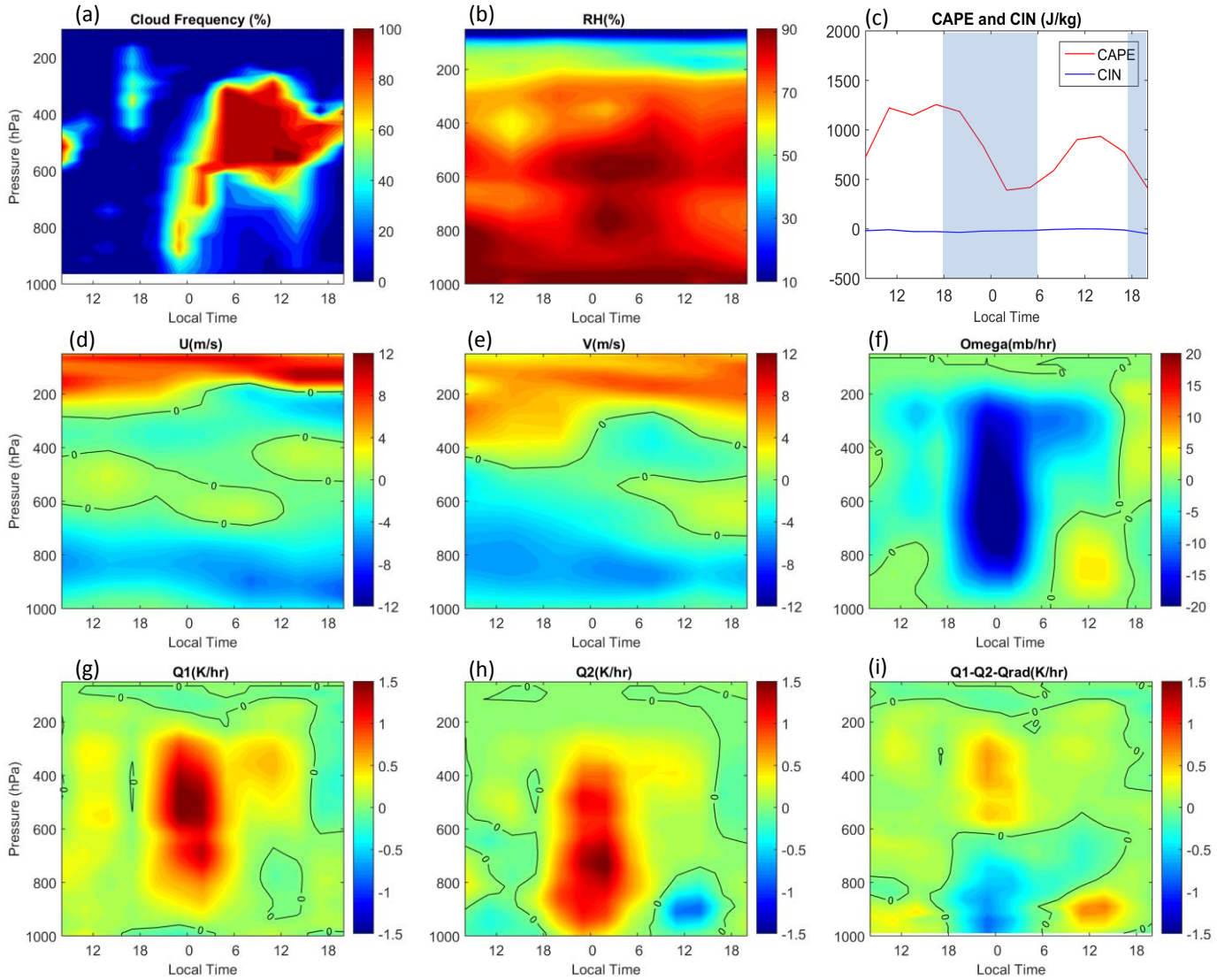
792

793

794

795

BOS (1 – 2 March 2014)



796

797 Figure 12: Similar as Figure 10 but for the BOS case.

798

799